Electronic Supplementary Material (ESI) for Physical Chemistry Chemical Physics.

Charge carrier mobilities in organic semiconductors: Crystal engineering and the importance of molecular contacts

Asif Bashir[1], Alexander Heck[4,5], Akimitsu Narita[2], Xinliang Feng[2], Alexei Nefedov[3], Michael Rohwerder[1], Klaus Müllen[2], Marcus Elstner[4,5], Christof Wöll[3]

[1]Max-Planck-Institut für Eisenforschung GmbH, 40237 Düsseldorf

[2]Max-Planck Institute for Polymer Research, 55128 Mainz

[3]Institute of Functional Interfaces, Karlsruhe Institute of Technology, 76344 Eggenstein-Leopoldshafen

[4]Institute of Physical Chemistry, Karlsruhe Institute of Technology, 76131 Karlsruhe

[5] HEiKA – Heidelberg Karlsruhe Research Partnership, Heidelberg University, Karlsruhe Institute of Technology (KIT); Germany

Supplementary information

In this study, different derivatives of hexa-*peri*-hexabenzocorononene (HBC) were used. This planar, fully conjugated hydrocarbon (Fig. S1) can be regarded as a small graphite unit and has proven as prototype of molecularly defined nanographenes.

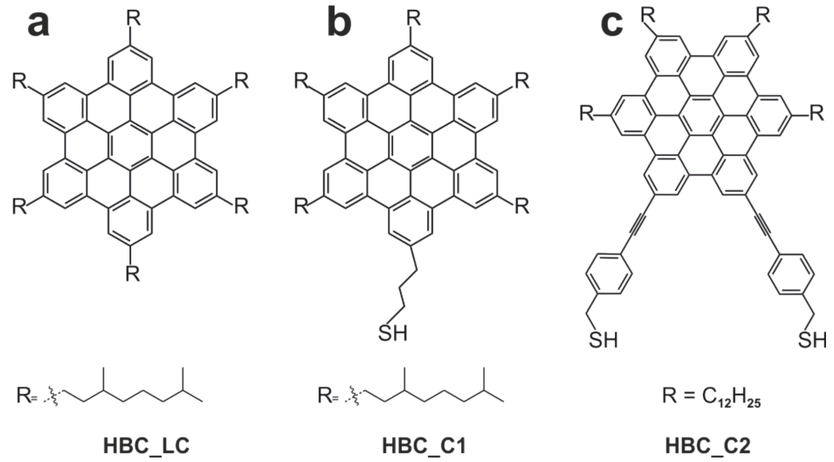

Figure S1: Molecular structure of hexa-*peri*-hexabenzocoronene and its derivatives. **a)** Liquid crystalline HBC derivate (HBC_LC), **b)** mono thiolate anchor (HBC_C1), and **c)** di thiolate anchor (HBC_C2).

Experimental Section

1.1 Preparation and characterization of 2,5-bis[4-(*S*-acetylthiomethyl)phenylethynyl]-8,11,14,17-tetrakis(n-dodecyl)hexa-*peri*-hexabenzocoronene (**3**)

2,5-Bis[4-(*S*-acetylthiomethyl)phenylethylnyl]-8,11,14,17-tetrakis(n-dodecyl)hexa-*peri*-hexabenzocoronene (**3**) was prepared through Sonogashira coupling of 2,5-dibromo-8,11,14,17-tetrakis(n-dodecyl)hexa-*peri*-hexabenzocoronene (**1**) [1] with 1-[4-(*S*-acetylthiomethyl)phenyl]acetylene (**2**) [2] in a similar manner to a reported procedure [3] (Figure S2). Matrix-assisted laser desorption/ionization time-of-flight (MALDI-TOF) mass spectrometry (MS) and ^{1}H NMR analyses proved the successful formation of compound **3** (Fig. S3). Notably, isotopic distribution of **3** displayed by the MALDI-TOF MS analysis was in perfect agreement with the simulated pattern, which provided a valid structural proof (Fig. S3, inset).

^{1}H NMR (500 MHz, 1,1,2,2-tetrachloroethane-d_2, 373 K): δ 8.70–8.25 (m, 12H, aryl-*H*), 7.79 (d, 4H, aryl-*H*), 7.43 (d, 4H, aryl-*H*), 4.26 (s, 4H, -S-CH_2), 3.30–3.10 (m, 8H, α-CH_2), 2.42 (s, 6H, -CO-CH_3), 1.85–1.10 (m, 80H, -CH_2-), 0.93–0.81 (m, 12H, -CH$_2$-CH_3).

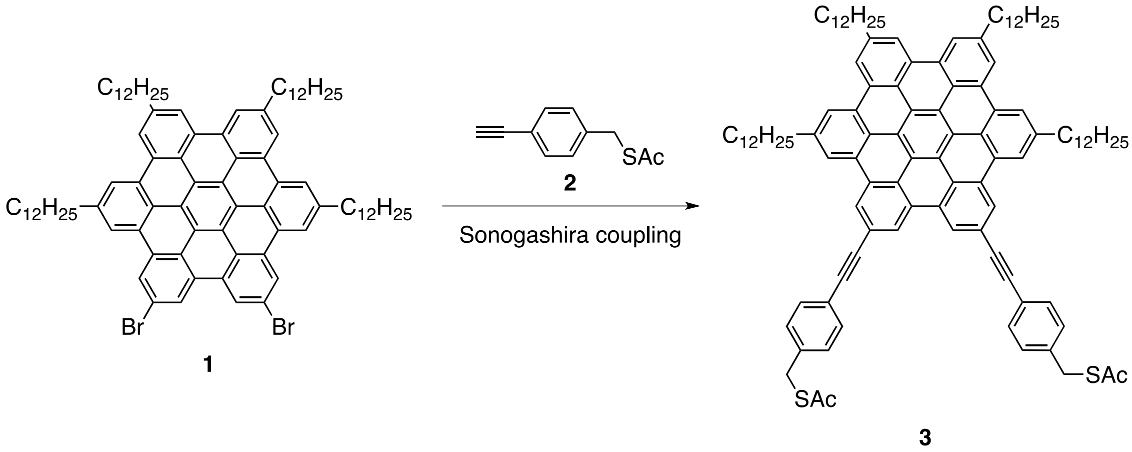

Figure S2. Synthesis of compound 3 through Sonogashira coupling.

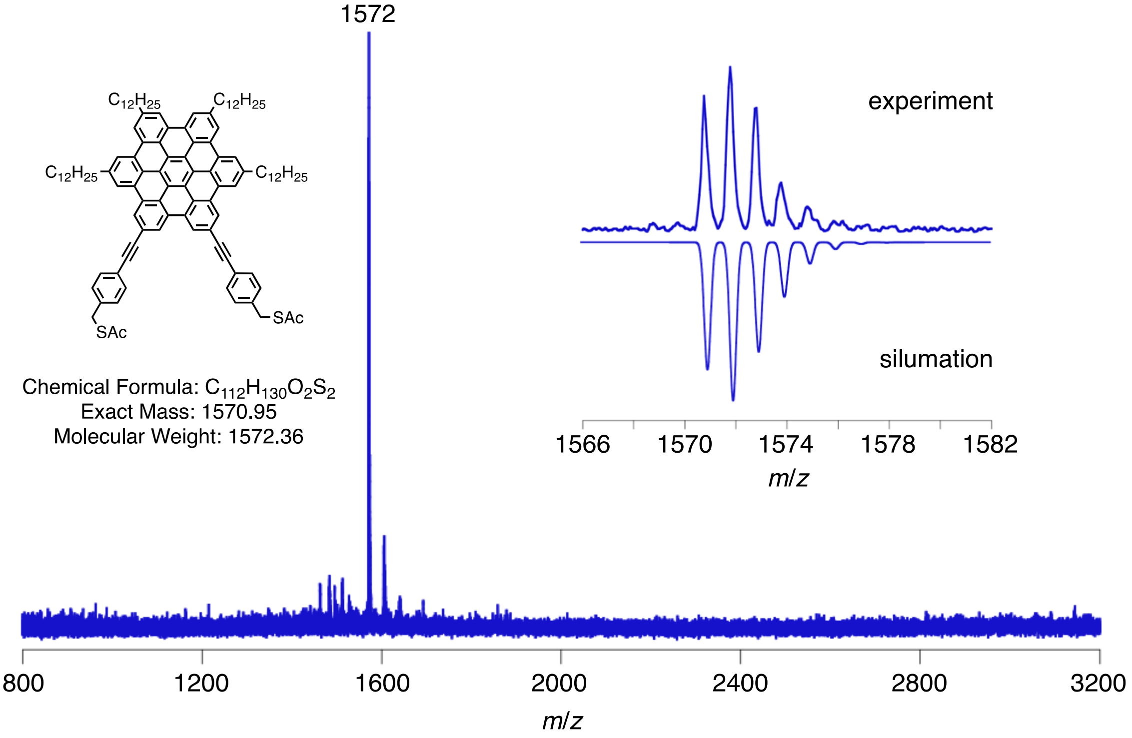

Figure S3: MALDI-TOF MS spectrum of compound **3**; inset: isotopic distribution of **3** in perfect agreement with the simulated pattern.

1.2 Molecular dynamic setup

For the Molecular Dynamics (MD) simulation of HBC derivatives the bonded parameters were obtained from the GAFF force field [4], whereas partial charges were fitted using CM3 computed from Density Functional Theory [5]. Every monomer was created with a random configuration of its stereogenic centers at the side chains.

HBC_LC was modeled as 9 columns consisting of 22 molecules each, arranged in a hexagonal lattice with slightly enlarged lattice constant to avoid superposition of atoms. The system was equilibrated with 10000 steps of conjugated gradient minimization followed by 1ns NVT equilibration at three different temperatures (400K, 450K and 500K

) using the Berendsen temperature coupling algorithm with T=0.2ps. The time step was 2fs and hydrogen bonds were constrained using the LINCS algorithm. An additional NPT equilibration was performed using semi-isotropic Berendsen pressure coupling with T_p=0.5ps, p_{ref}=1bar and a compressibility of $4{:}5 * 10^{-5}$ bar^{-1} for both directions. The production run was a 10ns simulation at the respective temperature using Nose-Hoover temperature coupling with T_p =3.0ps and semi-isotropic Parrinello-Rahman pressure coupling with T_p=3.0ps for both directions.

For HBC_C2 the anchoring atoms were kept fixed and the gold surface was not modeled explicitly, since in this upright orientation the molecules stand on their anchoring side chains, leaning on each other and therefore no significant interaction with the surface can be expected. The angle between the surface and the molecules correlates with the coverage of the surface, whereby the experimental NEXAFS angle of 65° is reproduced with a spacing of 3.9 Å between HBC_C2 molecules along the stack.

The same minimization and NVT equilibration protocol has been used, followed by a 10ns production run using Nose-Hoover temperature coupling with T_p =3.0ps. The reference temperature was 300K.

The temperature and pressure coupling used in the charge propagation simulation was the same as during the MD production runs, which generated the respective starting structures.

1.3 Calculation of electronic couplings

The electronic coupling between two molecules can be obtained in the fragment orbital approach as the Hamilton matrix element between the HOMOs φ^{HO} located at molecule i and j [6].

$T_{ij} = \langle \varphi_i^{HO} | \hat{H} | \varphi_j^{HO} \rangle$.

In the HBC molecule, however, the two highest occupied orbitals are degenerated and therefore an effective coupling can be derived arising from couplings between all four orbitals in Fig. 1b [7, 8]

Note, that in the direct propagation according to the time dependent Schrödinger equation all couplings were treated explicitly in the fragment orbital Hamiltonian (the three highest occupied orbitals were selected on every molecule).

1.4 Charge propagation simulations

The starting point for the simulation is the total energy expression of the charged (N-1 electron) system, which can be expanded as the energy of the charge neutral system minus the energy of one electron in the (over several molecules delocalized) HOMO orbital Ψ, corrected by electron relaxation effects given by a second order term E^{2nd}. [9-11]

$$E^{N-1}[\rho] = E^N[\rho_0] - \langle \Psi | \hat{H}_0 | \Psi \rangle + E^{2nd} \qquad (1)$$

Further, the energy of the neutral system $E^N[\rho_0]$ is very well described by the classical force field energy of the charge neutral system, therefore reducing the quantum mechanical problem to the energy of a missing charge carrier, which is given by the last two terms of eq. 1.

Next, the hole wave function Ψ is expanded in a set of relevant orbitals located on the molecular fragments. By exploiting the fact that the bonded interactions inside a molecule are much stronger than the interactions between two molecules, we can break down the costly self-consistent electronic calculation into two fast steps. First, we perform a QM calculation for each molecular fragment independently, embedded in the electrostatic environment generated by all surrounding atoms. Then, in a second step, we can use a combined set of fragment orbitals from all molecules to calculate the HOMO of the complex.

$$|\Psi\rangle = \sum_n a_n |\varphi_n\rangle \qquad (2)$$

As long as every fragment orbital is considered in the sum, we will get the exact same results as from diagonalization of the electronic problem in the usual atomic basis, but also for the same computational cost. However, we need only a few of the highest fragment orbitals to sufficiently describe the HOMO of the complex, since strongly bound fragment orbitals do not contribute to the global HOMO. Usually the HOMOs of the individual molecules are sufficient to describe the HOMO of the complex [10].

For the current system the expansion is performed in the set consisting of the three highest occupied orbitals of each HBC molecule, since the two highest MOs of HBC are degenerated and the HOMO-2 was included to be on the safe side.

The fragment orbitals φ_n are computed at every step of the MD from atomic orbitals using DFTB as quantum method [9], which gives couplings that agree very well with those computed with higher level methods at a fraction of cost [12].

The total energy expression of eq. 1 can then be expressed in this fragment orbital basis as

$$E^{N-1}[\rho] = E_o^{MM} - \sum_{mn} a_m a_n \langle \varphi_m | \hat{H}_0 | \varphi_n \rangle + \frac{1}{2} \sum_{mn} |a_m|^2 |a_n|^2 \Gamma_{mn} \qquad (3)$$

where the diagonal elements H_{nn} of the Hamiltonian are the MO energies, which can be related the ionization potentials (IP) of the respective HBC molecules, while the off-diagonal elements H_{mn} (for $m \neq n$) are the electronic couplings, which determine the probability of transfer between the MOs located at different molecules. $\Gamma_{mm} = U_m$ is the Hubbard parameter of orbital m, which covers relaxation effects of the orbital after charging the system. The off-diagonal terms Γ_{mn} are interactions of charges on neighboring sites and obtained from their inverse distance.

Please note, that this Hamiltonian includes the QM/MM coupling to the environment and furthermore, that during the MD the classical charges are effectively updated with Mulliken charges derived from the instantaneous hole wave function, which has an effect on the atomic dynamic via the potential energy $E^{N-1}[\rho]$ in eq. 5.

The simultaneous propagation of the hole wavefunction and the nuclear motions of the system is achieved by applying the Lagrangian formalism to the total energy expression. This leads to the time-dependent Schrödinger equation for the dynamic of the hole wave function:

$$i\hbar\dot{\Psi} = \hat{H}\Psi \qquad (4)$$

which can also be expressed in the basis of monomer orbitals (eq. 4) leading to:

$$i\hbar\dot{a}_m = \sum_n a_n\langle\varphi_m|\hat{H}|\varphi_n\rangle \qquad (5)$$

where $\hat{H}$ results from the last two terms of eq. 1.

$$\langle\varphi_m|\hat{H}|\varphi_n\rangle = -\langle\varphi_m|\hat{H}_0|\varphi_n\rangle + \delta_{mn}\sum_k \Gamma_{km}|a_k|^2$$

Analogously Newton-like expressions for the classical motion of the atoms α can be derived

$$ma_\alpha = -\frac{\partial E^{N-1}[\rho]}{\partial R_\alpha} \qquad (5)$$

which are propagated simultaneously with the electrons .

The derivation of the energy according to eq. 5 includes derivation of the Hamiltonian matrix elements H_{mn} that are tedious to calculate and not yet implemented in the current version of our code. However, for distant atoms these terms reduce to an additional coulomb term that can be efficiently evaluated by adding mulliken charges arising from the hole wavefunction to the force field atomic charges. This enables the environmental response to the moving charge that is labelled external reorganization energy in hopping models like Marcus theory [13-16].

While the interaction with the environment is well described by the updated atomic charges, the internal reorganization energy, which is the relaxation of a molecule after getting charged, is not sufficiently captured by this approach. Therefore, in our method this energy is precalculated and added as further charge dependent term to the Hamiltonian

$$E_{relax} = \sum_{m} \lambda_i \, \Delta q_m^2$$

Where $\Delta q_m = |a_m|^2$ is the occupation of fragment orbital *m* and λ_i is the internal reorganization energy of a single molecule.

Additionally, the electronic polarization of the environment for a charge carrier on site *n* was described by a polarizable continuum model according to the Born equation and added as additional charge dependent term to the Hamiltonian.

$$\Delta E_{solve}^{n} = -\frac{1}{4\pi\varepsilon_0}\frac{1}{2R}\left(1 - \frac{1}{\varepsilon_\infty}\right)\Delta q_n^2$$

Where ε_∞ is the optical permittivity of the system and R is the radius of the spherical approximated site.

The system specific parameters employed in our calculations are $\varepsilon_\infty = 2.0$ and R=0.7nm. Furthermore, we used for the reorganization energy (λ_i) 0.044eV, which was calculated at the B3LYP/def2-TZVP level and taken as average over the three considered fragment orbitals of HBC. The Hubbard parameter (U=3.02eV/e^2) was applied to all considered orbitals and was calculated as second derivative of the DFTB total energy with respect to the charge.

1.5 STM measurements

The STM data obtained from the HBC_C2 SAMs prepared at 298K presented in Fig. S4 (a-b) reveals the poor and ill-defined surface structure. No significant improvement in the surface morphology was observed upon the formation of HBC_C2 SAMs at 333K shown in Fig. S4 (c-d). The STM images show the appearance of high density of vacancy islands (etch pits) with poor order lamellar rows.

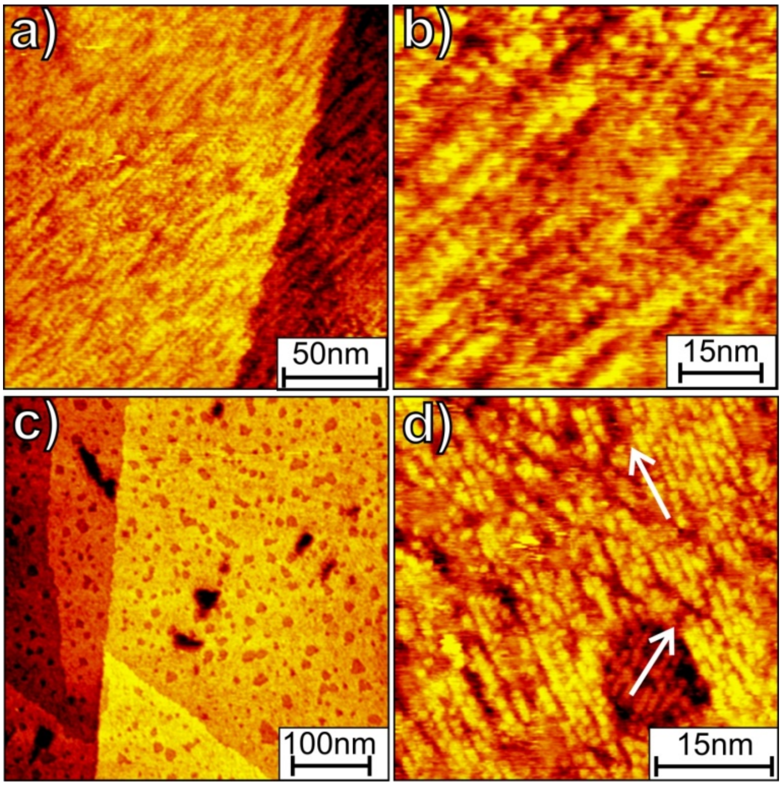

Figure S4: The summary of constant current STM images of HBC_C2 SAMs prepared at 298K and 333K on Au(111). **(a-b)** STM micrograph reveals the formation of HBC_C2 SAMs at RT forming the ill-defined structures distributed over Au(111). **(c-d)** STM micrograph reveals the formation of HBC_C2 SAMs at 333K forming short ordered lamellar rows on Au(111). These rows are rotated by 60° (white arrows in **d**) following the symmetry of underneath Au surface.

It has been reported that HBC-C10 dithiolate arrange in the edge-on fashion forming the poor and disorder wormlike structures on Au(111), unless the STM measurement carried out at the liquid/solid interface [17]. To this end, the HBC_C2 SAMs were prepared by immersing the gold substrates into ethanolic solution of HBC_C2 molecules for about 24 hours followed by the rinsing and drying processes. A fresh droplet of n-tetradecane is finally deposited on the HBC_C2 SAMs for the STM measurement at liquid/solid interface. Unfortunately, by employing the same procedure to fabricate the HBC_C2 SAMs results in the formation of poor and disorder wormlike structures as shown in Fig. S5.

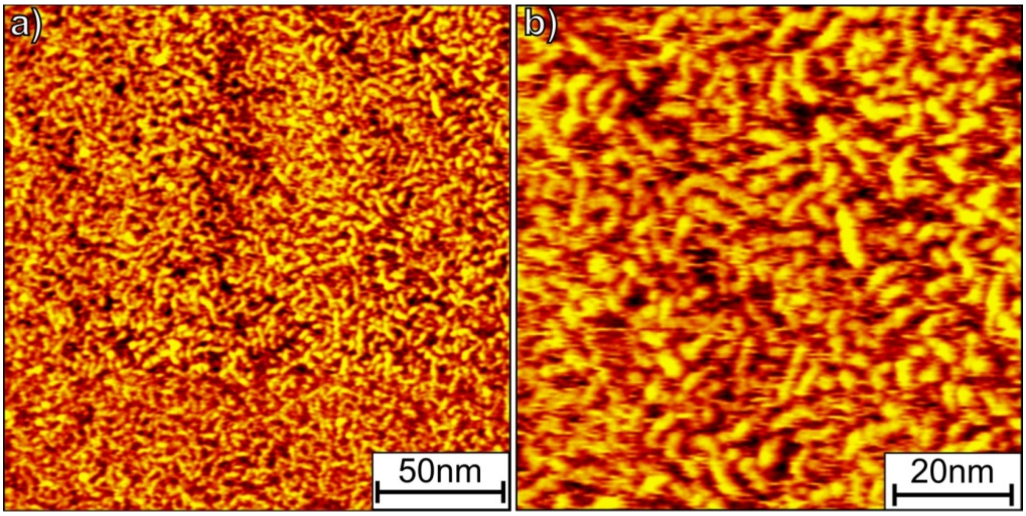

Figure S5: The constant current STM images of HBC_C2 SAMs on Au(111) at tetradecane/Au interface. a) Large scale micrograph reveals the formation of di-thiol HBC SAMs forming the less ordered wormlike structures distributed over Au(111) randomly. b) High resolution STM micrograph clearly showing the wormlike structures.

1.6 NEXAFS measurements

In order to characterize the molecular orientational ordering in HBC_C2 SAMs prepared at intermediate potential range E= -400 mV $_{(\mathrm{Ag/AgCl})}$ under UPD NEXAFS measurements were carried out. In Fig. S6 we present C1s NEXAFS spectra recorded for HBC_C2 SAMs at different angles of incidence. All spectra exhibit a number of characteristic absorption resonances due to excitations from the respective core-levels into π* and σ* orbitals of the aromatic rings as well as into molecular orbitals of Rydberg character. In order to determine the molecular orientation from an analysis of the dichroism, we focus our attention mainly on these 1s->π*-resonances around 285 eV. C K-edge NEXAFS spectra reveal a pronounced dichroism, i.e. the variation of intensity in dependence on the angle of incidence. In the bottom panel of Fig. S6 the difference between normal (90°) and grazing incidence (20°) is shown. The strong positive signal for the 1s->π*-resonances clearly demonstrates an up-right orientation of these SAMs [18]. A more detailed analysis of this dichroism allows to determine the tilt angle of the molecules with respect to the substrate surface. For molecules adsorbed on a surface with an at least three fold symmetry, the relationship of the NEXAFS resonance intensity $I_{\pi*}$ of the 1s->π*-resonances transitions and the X-ray radiation incidence angle θ relative to the surface can be expressed as:

$$\mathrm{I}_{\pi *} \propto P.\cos^2\theta.\left(1-\frac{3}{2}\sin^2\alpha\right)+\frac{1}{2}\sin^2\alpha \qquad (6)$$

where P denotes the degree of polarization of the incident x-ray light and α the average tilt angle of the transition dipole moments (TDMs) governing the particular excitation with respect to the surface normal [18, 19]. The fit of the experimental data the C K-edge 1s- π* transition intensities with a use of the equation (6) presented by the line in Fig. S6 and yields value for the dithiolate-anchored HBC tilt angle α of 65°.

A comparison of the structure obtained for the HBC_C1 SAMs [20] (adapted from ref 16) with the di-thiolate anchored one reveals that, as expected, the structure of the nanographene – SAMs resulting from the adsorption of the di-thiol anchors HBC cores is rather different. A structural model derived from the STM data and the NEXAFS data shown in Fig. 2. Compared to the structure of the HBC cores in the single thiol anchored case the relative tilt angle between the HBC cores form the surface normal is reduced to 25° whereas the distance between the HBC cores is roughly constant which is around 5 Å, thus yielding the area per molecules to 75 Å^2.

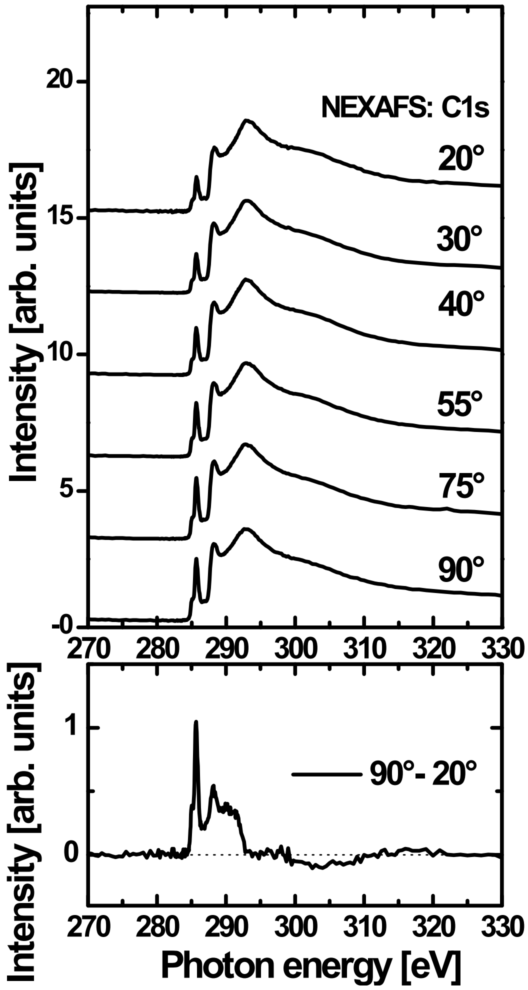

Figure S6: A series of NEXAFS C K-edge spectra of UPD HBC_C2 SAMs recorded at different incident angles (20°, 30°, 40° 55°, 75° and 90°). Bottom panel: the difference of the NEXAFS spectra recorded at normal (90°) and grazing (20°) incidence angles.

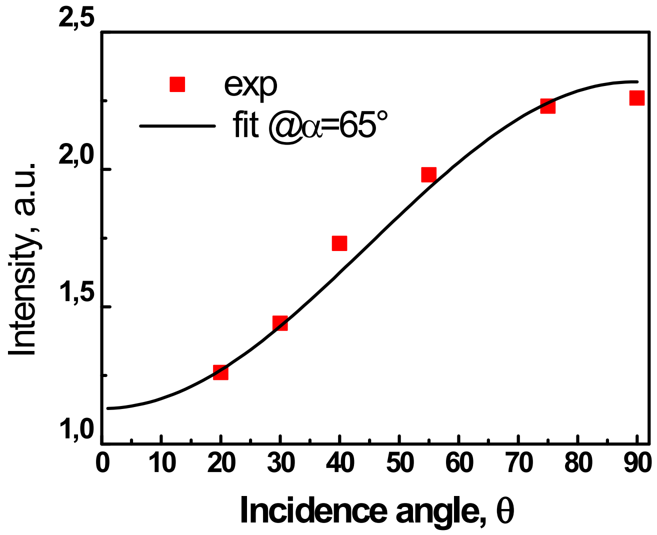

Figure S7: The angle dependence of the first π^* resonance intensity recorded for UPD HBC_C2 SAMs: the solid squares are the experimental data, line is the fitting using equation 1 with $\alpha = 65°$.

1.7 Fitting of width vs. height correlation HBC islands.

The previously established model[20] displayed in equation 7 was empirically modified for the current system to yield a charge carrier mobility HBC_C2 = 6.7 cm^{2}V^{-1}s^{-1}, significant higher than a value obtained for HBC_C1 = 4.2 cm^{2}V^{-1}s^{-1}.

$$width = \frac{P*0.5\,(R_{tn} - R_{HBC} - C'(d_{gap}+\Delta h)e^{\alpha(d_{gap}+\Delta h)})}{\frac{1}{3}R_{lat}\left(1-\frac{R_{tn}}{R_{HBC}}\right) - R_{tn} + \left(\frac{1}{3}\frac{R_{lat}}{R_{HBC}}+1\right)\cdot C'(d_{gap}+\Delta h)e^{\alpha(d_{gap}+\Delta h)}} \qquad (7)$$

The above equation has been derived in detail previously[20] where: R_{tn}, R_{HBC}, d_{gap}, and C′ are resistance of network, resistance of HBC molecules, vacuum gap and constant respectively. The pre-factor P was fixed at a value of 10 and is introduced to optimize the empirical fit and is a consequence of the difference between the geometry of the single anchor (HBC_C1) and double anchor (HBC_C2) molecule.

1.8 Fitting of simulated mobilities

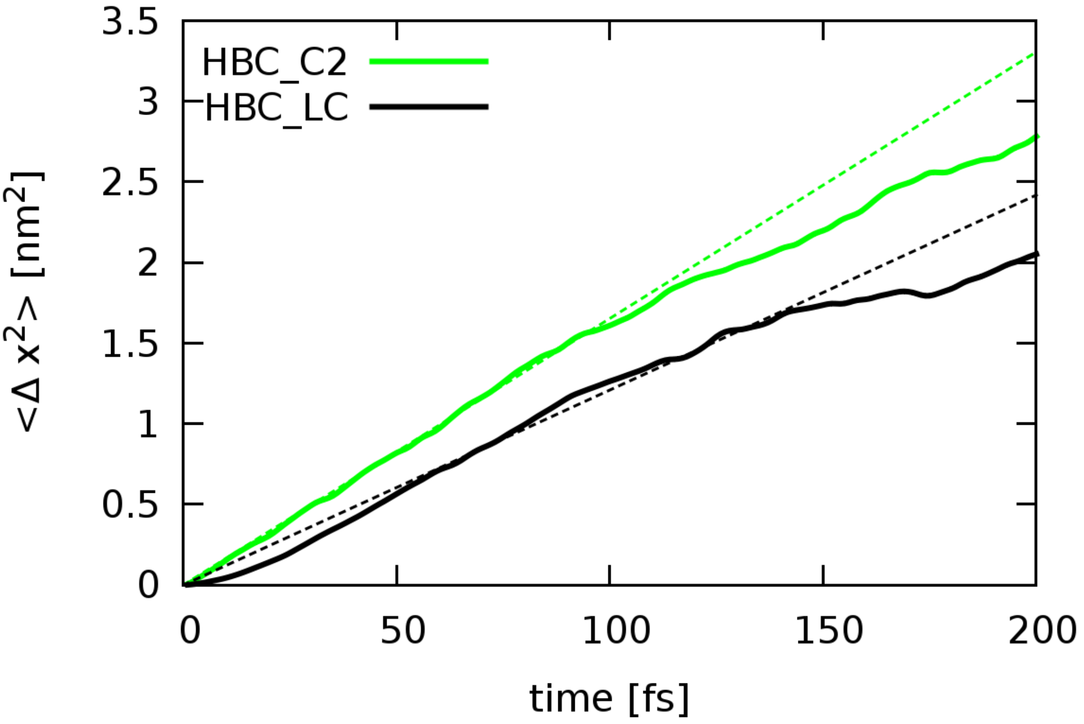

Figure S8: Linear fit of the mean square displacement of the charge carrier over the first 100fs of the Ehrenfest simulations. Deviations at longer timescales are due to the finite number of molecules in the simulation.

References

1. S. Ito, M. Wehmeier, J. D. Brand, C. Kubel, R. Epsch, J. P. Rabe and K. Müllen, *Chem-Eur J*, 2000, **6**, 4327-4342.
2. D. T. Gryko, C. Clausen, K. M. Roth, N. Dontha, D. F. Bocian, W. G. Kuhr and J. S. Lindsey, *J. Org. Chem.*, 2000, **65**, 7345-7355.
3. P. Angelova, H. Vieker, N. E. Weber, D. Matei, O. Reimer, I. Meier, S. Kurasch, J. Biskupek, D. Lorbach, K. Wunderlich, L. Chen, A. Terfort, M. Klapper, K. Müllen, U. Kaiser, A. Golzhauser and A. Turchanin, *ACS Nano*, 2013, **7**, 6489.
4. J. M. Wang, R. M. Wolf, J. W. Caldwell, P. A. Kollman and D. A. Case, *J. Comput. Chem.*, 2004, **25**, 1157-1174.
5. J. A. Kalinowski, B. Lesyng, J. D. Thompson, C. J. Cramer and D. G. Truhlar, *J. Phys. Chem. A*, 2004, **108**, 2545-2549.
6. K. Senthilkumar, F. C. Grozema, F. M. Bickelhaupt and L. D. A. Siebbeles, *J. Chem. Phys.*, 2003, **119**, 9809-9817.
7. M. D. Newton, *Chem Rev*, 1991, **91**, 767-792.
8. J. Kirkpatrick, V. Marcon, K. Kremer, J. Nelson and D. Andrienko, *J. Chem. Phys.*, 2008, **129**.
9. T. Kubar and M. Elstner, *J. Phys. Chem. B*, 2010, **114**, 11221-11240.
10. T. Kubar and M. Elstner, *J. R. Soc. Inter.*, 2013, **10**, 1-18.
11. T. Kubar and M. Elstner, *Phys. Chem. Chem. Phys.*, 2013, **15**, 5794-5813.
12. A. Kubas, F. Hoffmann, A. Heck, H. Oberhofer, M. Elstner and J. Blumberger, *J. Chem. Phys.*, 2014, **140**.
13. R. A. Marcus, *J. Chem. Phys.*, 1956, **24**, 966-978.
14. R. A. Marcus, *J. Chem. Phys.*, 1956, **24**, 979-989.
15. R. A. Marcus, *Annu. Rev. Phys. Chem.*, 1964, **15**, 155-&.
16. R. A. Marcus and N. Sutin, *Biochim. Biophys. Acta*, 1985, **811**, 265-322.
17. L. Piot, C. Marie, X. Dou, X. Feng, K. Müllen and D. Fichou, *J. Am. Chem. Soc.*, 2009, **131**, 1378-1379.
18. A. Nefedov and C. Wöll, *Springer Series in Surface Science*, 2013, **51**, 277-306.
19. J. Stöhr, „NEXAFS Spectroscopy“, *Springer Verlag, Berlin*, 1992,.
20. D. Käfer, A. Bashir, X. Dou, G. Witte, K. Müllen and C. Wöll, *Adv. Mater.*, 2010, **22**, 384-388.